High-resolution x-ray emission spectrometry in the lithium K range with a reflection zone plate spectrometer

Khalil Hassebi, Nicolas Rividi, Michel Fialin, Anne Verlaguet, Gaston Godard, Jürgen Probst, Heike Löchel, Thomas Krist, Christoph Braig, Christian Seifert, et al.

High-resolution x-ray emission spectrometry in the lithium K range with a reflection zone plate spectrometer

Khalil Hassebi[1], Nicolas Rividi[2], Michel Fialin[2], Anne Verlaguet[3], Gaston Godard[4], Jürgen Probst[5], Heike Löchel[5], Thomas Krist[5], Christoph Braig[6], Christian Seifert[6], Rabah Benbalagh[1], Régis Vacheresse[1], Vita Ilakovac[1,7], Karine Le Guen[1], Philippe Jonnard[1]

[1] Laboratoire de Chimie Physique—Matière et Rayonnement, Faculté des Sciences et Ingénierie, Sorbonne Université, UMR CNRS, 4 place Jussieu, 75252 Paris Cedex 05, France

[2] Service Camparis, UMS 7154—CNRS, OSU Ecce Terra, Sorbonne Université, 4 place Jussieu, 75005 Paris, France

[3] Sorbonne Université, CNRS-INSU, Institut des Sciences de la Terre de Paris, ISTeP UMR 7193, F 75005 Paris, France

[4] Université Paris Cité, Institut de Physique du Globe de Paris, 75005 Paris, France

[5] NOB Nano Optics Berlin GmbH, Krumme Str 64, 10627 Berlin, Germany

[6] Institute of Applied Photonics e. V., Rudower Chaussee 29/31, 12489 Berlin, Germany

[7] CY Cergy Paris Université, 95302 Cergy-Pontoise Cedex, France

Keywords: lithium, x-ray emission spectroscopy, reflection zone plate, wavelength dispersive spectrometry

Abstract

Implementing a newly developed spectrometer for the soft x-ray range of (35 – 130) eV based on reflection zone plates was successfully accomplished on an electron probe microanalyzer. In this context, we present the first spectra acquired using this setup, including those of elements such as Be (Kα), C (Kα), Mg ($L_{2,3}$), Al ($L_{2,3}$), and Si ($L_{2,3}$). We have also conducted an analysis of several lithium compounds and measured the emission of Li Kα from metallic Li, LiF, and $LiNbO_3$. Some of the results were compared with density functional theory calculations. The spectrum obtained for the lithium-bearing mineral amblygonite $Li_{0.75}Na_{0.25}Al(PO_4)F_{0.75}(OH)_{0.25}$ is chosen to discuss some of the challenges faced.

Introduction

The detection and quantification of lithium have always been challenging, due to several factors including the low fluorescence yield, strong re-absorption, low photon energy (Li Kα emission is in the 50 eV range), etc. Overcoming those challenges will contribute to progress in several fields, for instance, to develop better batteries (higher capacity, enhanced safety, …) by gaining insights on the occupied electronic states and their spatial distribution. Over the past few years, a growing body of literature started contributing toward achieving these goals. These contributions cover both theories by computing the density of states and Li K emission band using ab initio-based calculations [1], [2], as well as experiments through the measurement of the lithium x-ray emission in various compounds [2], [3], [4]. A considerable portion of these experiments has been performed on an electron probe microanalyzer (EPMA) due to its accessibility.

The ongoing development of EPMA from the first instrument reported by Castaing and Guinier in 1949 [5], to the more advanced ones equipped with field-emission electron guns (FEG) and the latest generations of energy (EDS) and wavelength dispersive spectrometers (WDS), allows the analysis of traces and light elements down to beryllium with a high spatial resolution reaching the microscale and even nanoscale (as low as 40 nm) with the use of FEG on thin samples [6]. It also allows a high spectral resolution of about 0.2 eV measured at the Al L edge for a grating-based WDS spectrometer [3]. All this led to its continuing use in the fields of science and industry.

X-ray emission spectroscopy (XES) attracts considerable interest because of its capability to analyze the structural and electronic properties of materials by probing the valence density of states [7]. The emission can either consist of atomic lines (transition between two electronic core states) or emission bands (transitions between the valence band and a core hole). The core hole makes the emission characteristics of the emitting element, and involvement of the valence band gives to the method its chemical state sensitivity, while the dipole nature of the electron transition provides information on the symmetry of state [8]. XES analysis then allows determining the sample elemental composition and producing chemical maps with the spatial distribution of elements. Up to now however, lithium remains out of the scope of EPMA XES when it is present in complex materials such as silicates, as overlaps with high diffracted order emissions of the other elements can occur, beside the strong matrix effect [1].

There were few attempts to use non-destructive techniques such as EDS to detect lithium in metallic lithium [9] and also binary lithium compounds (LiH, Li_3N, Li_2S, LiF, and LiCl) [10]. However, the low spectral resolution of EDS prevents it from giving information on the chemical state of the lithium atoms and can give a false interpretation in the presence of elements that emit close to the lithium emission band. That is the reason why in our research we will exclusively utilize WDS because this technique has shown to be efficient in detecting Li K emission. For example, Aita *et al.* applied WDS to successfully detect and acquire the Li K emission in lithium metal [11]. The x-rays were generated by electron ionization and collected with a grazing incidence spectrometer with a concave grating in the Rowland mounting. With the evolution of gratings, a more advanced grating, this time based on varied-line-spacing (VLS) flat-field optics, was used within a transmission electron microscope (TEM) by Terauchi *et al.* to measure lithium emission in the 5% Li-Al alloy [3]. Then, the combination of these spectrometers with EPMA, which benefits from a high beam current compared to TEM, allowed Takahashi *et al.* to detect and more effectively resolve the Li K emission in Mg-Li-Ca alloy, lithium metal, LiF, and in Li-Al alloy [4].

A WDS based on the use of a reflection zone plate (RZP) of laminar type that uses a two-dimensional array of elliptical grooves working as a VLS grating has been first reported by Erko *et al.* [12], [13] and followed in several other papers [14], [15], [16]. VLS gratings are diffractive optical elements for spectroscopy with focusing capability provided by a continuous variation of the line density in the dispersive direction. The line density distribution across the aperture of the VLS grating is critical for its optical quality, in terms of the achievable energy-dependent resolution. RZP are special 2D VLS gratings. In the sagittal direction, the grating lines of our RZP are weakly curved, and their density increases slowly [17]. Hence, a wide aperture can be realized, yielding a high photon flux. Based on the precise calculation of the grating line density distribution via the optical path length, the RZP maintains a flat focal line close to the diffraction limit. In addition, a spherical substrate minimizes chromatic aberrations over a wide energy range [16].

A spectrometer based on a RZP covering the range of (35 – 130) eV will be used in our research. In this paper, we present the new setup and first tests of the RZP spectrometer mounted on EPMA, particularly the spectra obtained in the Li K range which includes Li metal, LiF and $LiNbO_3$.

Methods

Reflection zone plate spectrometer

The spectrometer used in the experiment is the WDSX spectrometer manufactured by NOB Nano Optics Berlin GmbH. It consists of a RZP and a back-illuminated CCD camera (Greateyes). The RZP is the diffractive component of the spectrometer. Its working principle (see Fig. 1) was already discussed in a paper by Erko et al. [12]. The Fresnel zones were calculated specifically based on the exact setup geometry and the desired energy range and spectral resolution. The zone structure was transferred onto a curved silicon substrate via laser lithography. For the final coating, carbon was chosen to optimize the diffraction efficiency. The values of the main parameters of the RZP are collected in Table 1. The RZP is 40 mm long and has a trapezoidal shape, with its width varying from 8.1 mm to 10.6 mm. The RZP contains 7640 grooves or lines.

Table 1: Parameters of the reflection zone plate and of the geometry of the experiment.

Entrance arm length R_1	150 mm
Exit arm length R_2	150 mm
Entrance angle α	2.65°
Exit angle β, at 53 eV (design energy)	6°
Curvature radius of the spherical substrate	4 m
Central grating period d	5.306 µm
Profile depth	78 nm
Coating	Carbon 10 nm

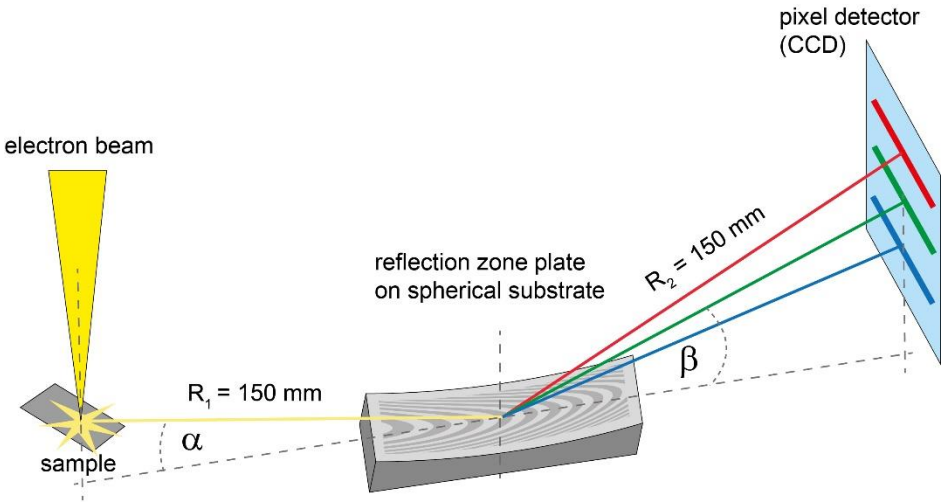

Figure 1: Schematic of the setup geometry inside the spectrometer.

In a RZP, the number of lines along the beam direction governs the diffractive properties over the accessible energy range of the spectrometer and thereby the theoretical spectral resolution, which is in reality usually limited by the source size and the pixel size of the detector. The different energies are simultaneously focused to straight lines (see Fig. 1) at different positions on the x-ray CCD camera according to the grating law expressed by:

$$d(cos\,\alpha - cos\,\beta) = m\lambda \tag{1}$$

with α and β being the glancing incident (or entrance) and diffraction (or exit) angles, respectively, defined for the m^{th} order of wavelength λ, and d being the mean spacing of the grating grooves.

The factors influencing spectral resolution include the geometrical magnification of the source, the diffraction limit, chromatic aberrations, and the spatial resolution of the CCD. In our case, particularly in the range of 48.5 – 56.5 eV around the design energy, the resolution is primarily limited by the detector. For the chromatic aberration, Fig. 2 illustrates the variation in the width of the focal line on the CCD camera as a function of the photon energy. This contribution is minimal between 50 and 55 eV and becomes more important at higher photon energies.

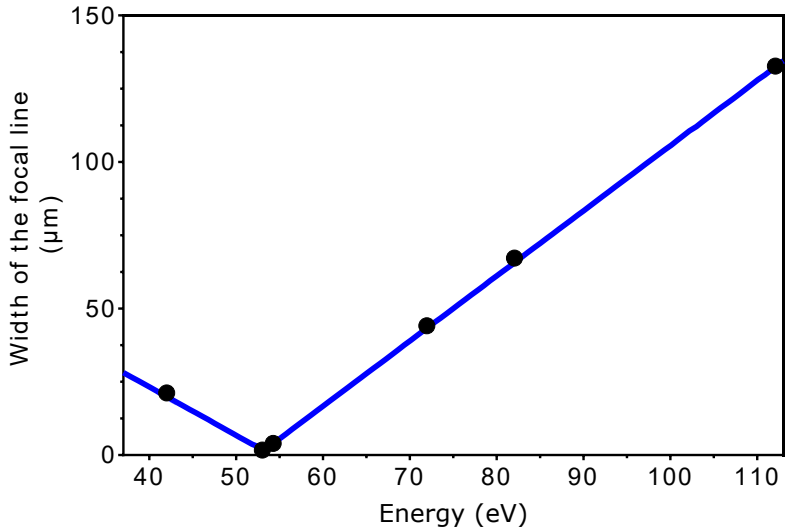

Figure 2: simulation of the chromatic aberration as a function of the photon energy. The blue line is a guide to the eye.

The radiation dispersed by the RZP is detected by the CCD camera with a pixel size of 13.5 µm x 13.5 µm and an image format of 2048 x 515 pixels. The radiation is dispersed along the 515 pixels, each of these pixels representing a different wavelength. The pixel columns along the long side of the CCD area (2048 pixels), which is illuminated by the line focusing RZP, are integrated for each of the 515 pixel rows to obtain a spectrum. The acquisition speed of the camera used to measure our spectra were 1 MHz or 50 kHz. The lower acquisition speed enables decreasing the reading noise, and thus the background under the spectra. This mode was used when the measured intensity of the emission is low.

The spectrometer is used without a window by employing a 3D-printed adaptive tunnel (Fig. 3) to connect it to the secondary vacuum in the analysis chamber directly, instead of relying on the primary vacuum provided usually for EPMA spectrometers in the Cameca SX 100. The tunnel was intended to create a differential pressure difference through its low conductance to reach the pressure required for the use of the CCD camera at -60°C. This allows to reach a pressure of 7×10^{-5} mbar, which is suitable to ensure the proper functioning of the CCD camera under low temperatures, while avoiding the formation of ice on it. The cooling of the CCD is necessary to lower the noise and to minimize the background.

Electron Probe Micro Analyzer

The Cameca SX 100 microprobe utilized in the experiment is equipped with a tungsten filament with acceleration voltages ranging from 0.5 to 30 kV and beam currents of 10 to 700 nA. The samples are mounted on an automated stage that has a precision better than 3 µm with a spot size less than a micrometer, enabling EPMA to analyze weights down to several ppm for selected elements. Figure 3 represents a simplified scheme of the EPMA at the CAMPARIS facility at Sorbonne Université, equipped with Johann-type spectrometers using crystals and multilayers and with the RZP spectrometer.

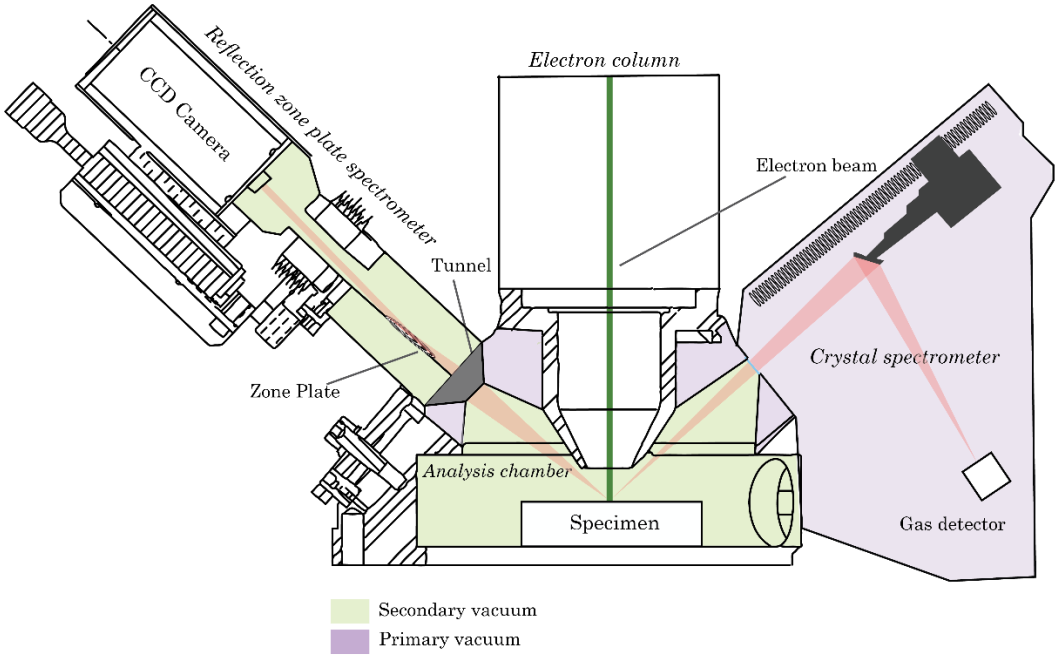

Figure 3: Simplified schematic of the Cameca SX 100 microprobe, equipped with crystal-based WDS and reflection zone plate spectrometer.

Data processing

First, the dark noise coming from the CCD camera is suppressed. For that purpose spectra without (dark) and with the electron beam are obtained both in the same conditions and the former is subtracted from the second spectrum. This procedure is important in case of faint emissions are expected. All the spectra measured by the spectrometer are affected by a background coming from the continuous spectrum of the decelerated electrons (so-called bremsstrahlung). To subtract this background from the final spectra, a baseline correction algorithm based on the asymmetrical least square method is used [18].

Example of spectra

From the viewpoint of spectral resolution and compared to the use of multilayers (few eV resolution), the RZP spectrometer has a high energy resolution that reaches 0.3 eV at the Al $L_{2,3}$ edge (72 eV, [19]) and 0.25 eV measured at the Mg $L_{2,3}$ edge (49 eV, [19]), as shown in the $L_{2,3}$ emission spectra (electron transition from the s and d valence states towards the $2p_{3/2,1/2}$ core level) presented in Fig. 4. Those values are defined as the energy difference between 75 % and 25 % of the maximum from the top to the background of the Fermi edge.

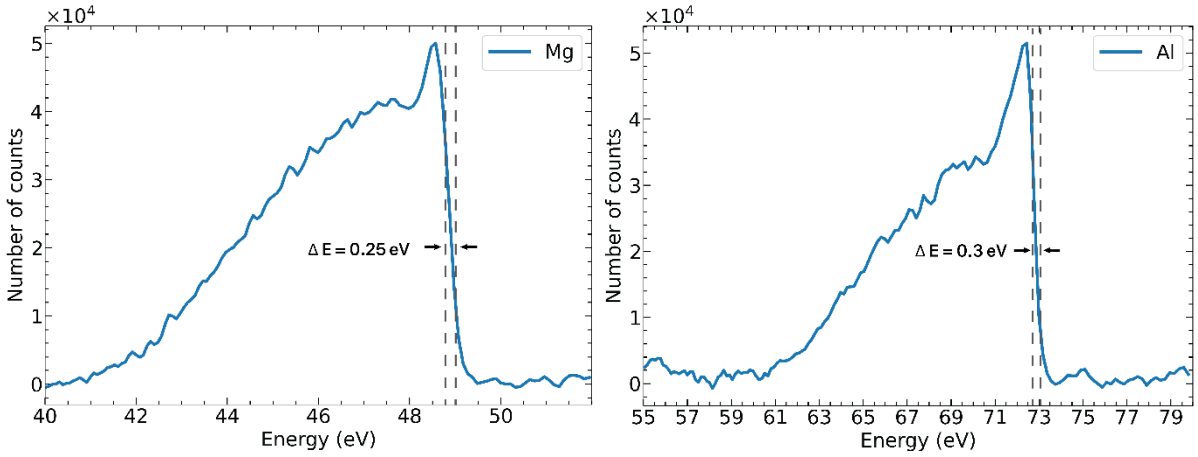

Figure 4: Mg $L_{2,3}$ emission of metallic magnesium and Al $L_{2,3}$ emission from aluminum.

The photon energy calibration of the RZP is made using of peaks from high order diffraction peaks of C Kα (electron transition from the p valence states towards the C 1s core level , 277 eV) emission from graphite, as shown in Fig. 5. This procedure is chosen because their positions are precisely known and cover the whole range of the spectrometer. We can note, Fig. 5(a), that the positions of the 5th and 6th diffraction orders fall in the Li K range (around 50 eV). We observe that the width of the carbon emission band decreases with the diffraction order increasing. This due to the fact that the dispersion is decreasing with diffraction order as it can be deduced from the grating law. If we plot the various diffraction peaks on the energy scale relative to the 3rd order diffraction, Fig. 5(b), then all peaks have similar width and shapes. Their differences come from the variation of the spectral resolution as a function of the photon energy, see Fig. 2. The seventh order peak is cut toward low energies because it occurs at the lower limit of the spectrometer.

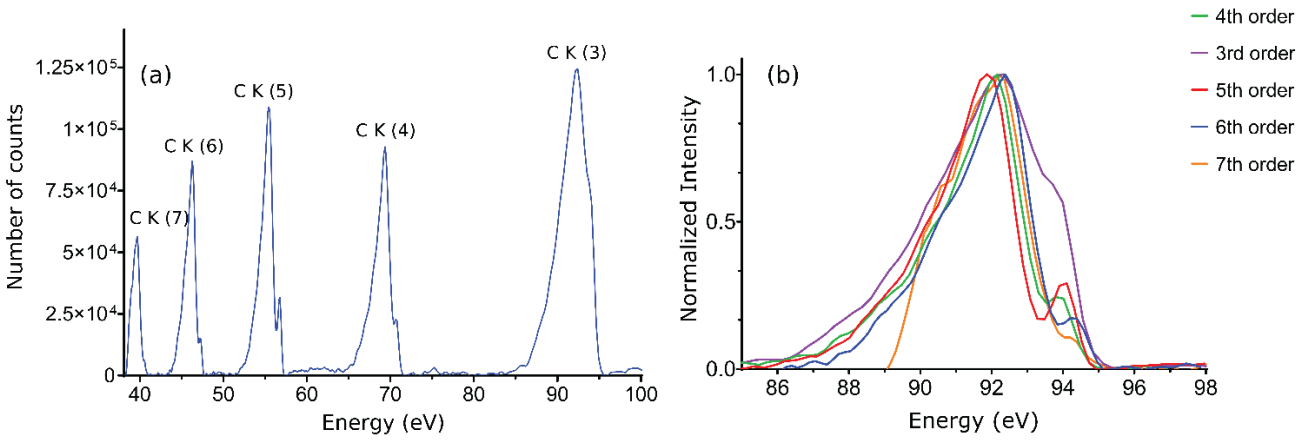

Figure 5: (a) High order diffraction peaks of C Kα emission in graphite across the full range of the spectrometer. The numbers in parentheses represent the diffraction orders; (b) high order peaks scaled to the photon energy scale of the 3rd order peak and normalized to their maximum.

To validate the calibration procedure, we compare spectra acquired for several materials including Mg, Al, Si and Be (Fig. 6) to the associated energy values from the literature [19], and the results are found to be in good agreement. These emission bands are about 10 eV wide. These widths originate from the natural widths of the emission and the experimental broadening. The natural widths themselves derive from the widths of the core levels and of the valence bands. Because the widths of the core levels and the experimental broadening are small, less than 0.1 eV, the observed widths of the emissions bands reflect the widths of the valence bands.

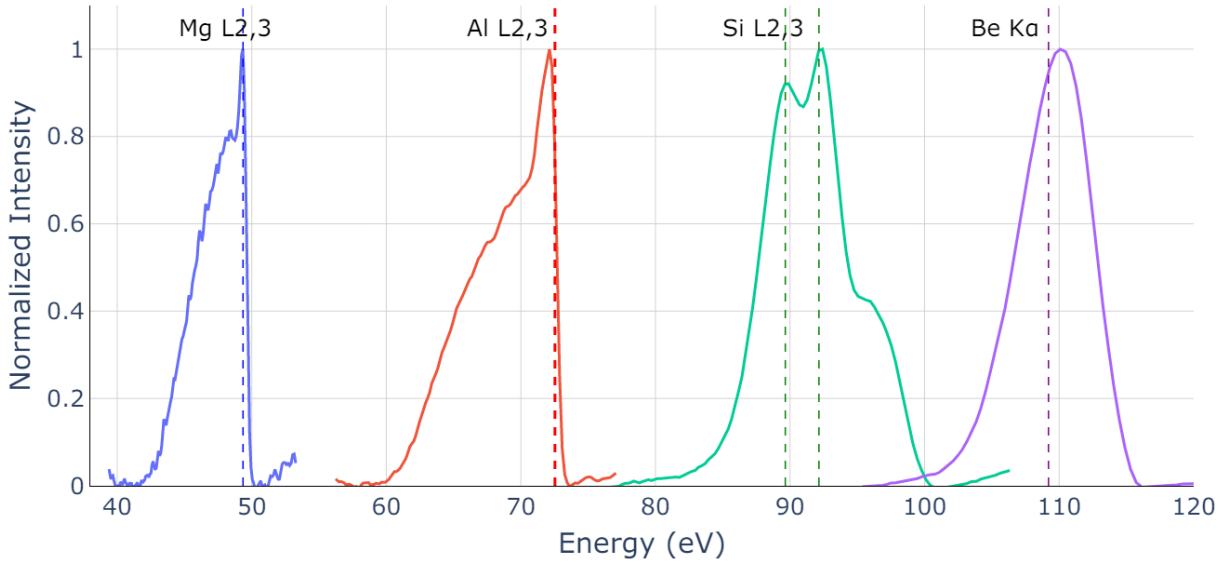

Figure 6: The x-ray emission bands of Mg $L_{2,3}$ of metallic Mg, Al $L_{2,3}$ of metallic Al, Si $L_{2,3}$ of pure silicon and Be Kα of metallic Be. The dashed lines represent the photon energies from the literature [19].

Attenuation lengths of the Li Kα emission

In Table 2 we present a comparison of the attenuation coefficients (which denote how easily a material can be penetrated by the beam of x-ray photons) and attenuation lengths (defined as the distance at which the intensity of the beam drops to 1/e of its initial value, for an emergence angle of 45° in our case) of the Li Kα emission in different compounds, including lithium oxide and spodumene. Values are deduced from the CXRO website (https://henke.lbl.gov/optical_constants/). The table shows that the Li Kα emission undergoes an important attenuation in the lithium compounds, represented by the increase of the attenuation

coefficient, reaching values larger by a factor of 100 compared to lithium metal. This substantial rise in the attenuation coefficient corresponds to a remarkable reduction in the attenuation length, changing from 1.8 µm in the case of lithium metal to few tens of nanometers in its other compounds.Consequently, the emission of only a small number of lithium atoms can be detected and thus we expect the intensity collected from non-metallic samples to be a few hundred times less intense than the one from Li metal.

Table 2: Comparison of the attenuation coefficients and attenuation lengths of different compounds [20]. (*) Empirical formula and density from the Mineralogy Database, http://webmineral.com/. The attenuation coefficient and attenuation length are specified at 50 eV and an emergence angle of 45°.

Material	Composition or empirical formula	Density (g/cm^3)	wt% Li	Attenuation coefficient (cm^{-1})	Attenuation length (nm)
Li	Li	0.53	100	3.85×10^3	1823
LiF	LiF	2.64	26.8	371×10^3	19
Li_2O	Li_2O	2.01	46.5	189×10^3	37
$LiNbO_3$	$LiNbO_3$	4.3	4.69	296×10^3	24
Spodumene	$LiAlSi_2O_6$	3.1	3.7	284×10^3	25
Lepidolite(*)	$KLi_2AlSi_4O_{10}F(OH)$	2.84	3.6	350×10^3	18
Amblygonite(*)	$Li_{0.75}Na_{0.25}Al(PO_4)F_{0.75}(OH)_{0.25}$	3.04	3.4	391×10^3	15
Bikitaïte(*)	$Li_2Al_2(Si_2O_6)_2 \cdot 2(H_2O)$	2.28	3.4	348×10^3	22

Results and discussion

- *Lithium metal*

We have studied a sample of pure lithium, kept under vacuum to avoid the oxidation. The sample surface was gently scratched in an attempt to remove any oxidized layers and quickly inserted into the analysis chamber. The sample was analyzed with an accelerating voltage of 5 kV, beam current of 100 nA and an acquisition time of 100 s. The spectrum features an asymmetric peak shape which is expected for such metal (Fig. 7). The Li Kα emission is centered at 54.3 eV and represents the transition from the *2p* valence states to the K shell. The spectrum also shows the presence of high diffraction orders from O Kα, caused by the oxidation of the surface while the film was exposed to air during its introduction into the microprobe. Moreover, Fig. 7 displays the comparison to the calculated spectrum using DOS calculations [1]. Calculations are performed with WIEN2k code [21] implementing a full-potential augmented plane wave method [22]. The approximation for the exchange-correlation function used is generalized gradient approximation of Perdew-Burke-Ernzerhof [23].The calculated spectrum, deduced from the valence DOS, was shifted by a value equal to the binding energy of the Li 1s core level at 54.78 eV, as determined by XPS [24]. The experimental spectrum and the calculations are in good agreement, the small discrepancies between both are attributed to the presence of carbon and oxygen contaminations, making it difficult to determine the background correctly.

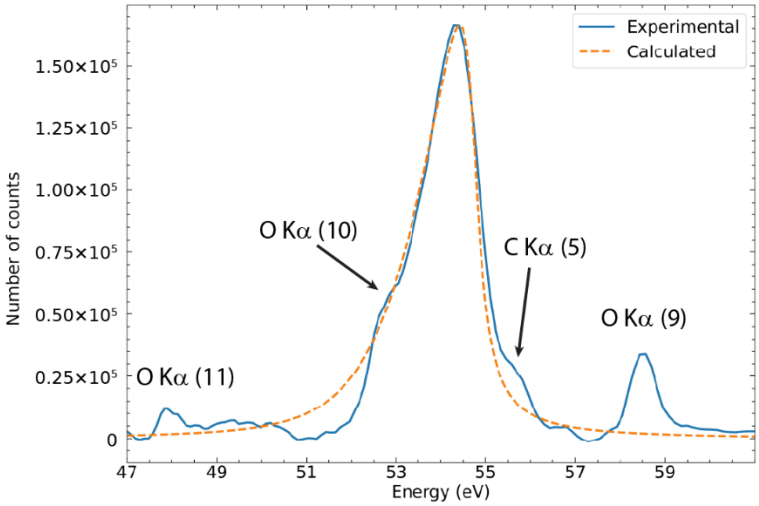

Figure 7: Experimental spectrum of lithium metal (blue) compared to the calculated one (orange, dashed), obtained in the range from 47 eV to 60 eV.

- *LiF sample*

A lithium fluoride sample was analyzed during this work. Usually, the sample surface is covered by a thin layer of graphite to ensure good conductivity and to avoid charging effects. To reduce the strong overlap between C Kα and Li Kα emission, carbon was not used as a coating material. Instead, we have employed a 5 nm layer of gold, as gold emissions do not overlap with Li Kα. Several measurements of soft x-ray emission spectra of Li Kα have been performed on LiF [4], [21 – 23], excited either by photons or electrons, with conflicting observations. This can be due to the rapid change of the spectra of halogen containing compounds under bombardment, which is influenced by the analysis conditions (number of incident particles, size of the incident beam and acquisition time). Some of these spectra have been collected in Fig. 8 and compared with our measurement.

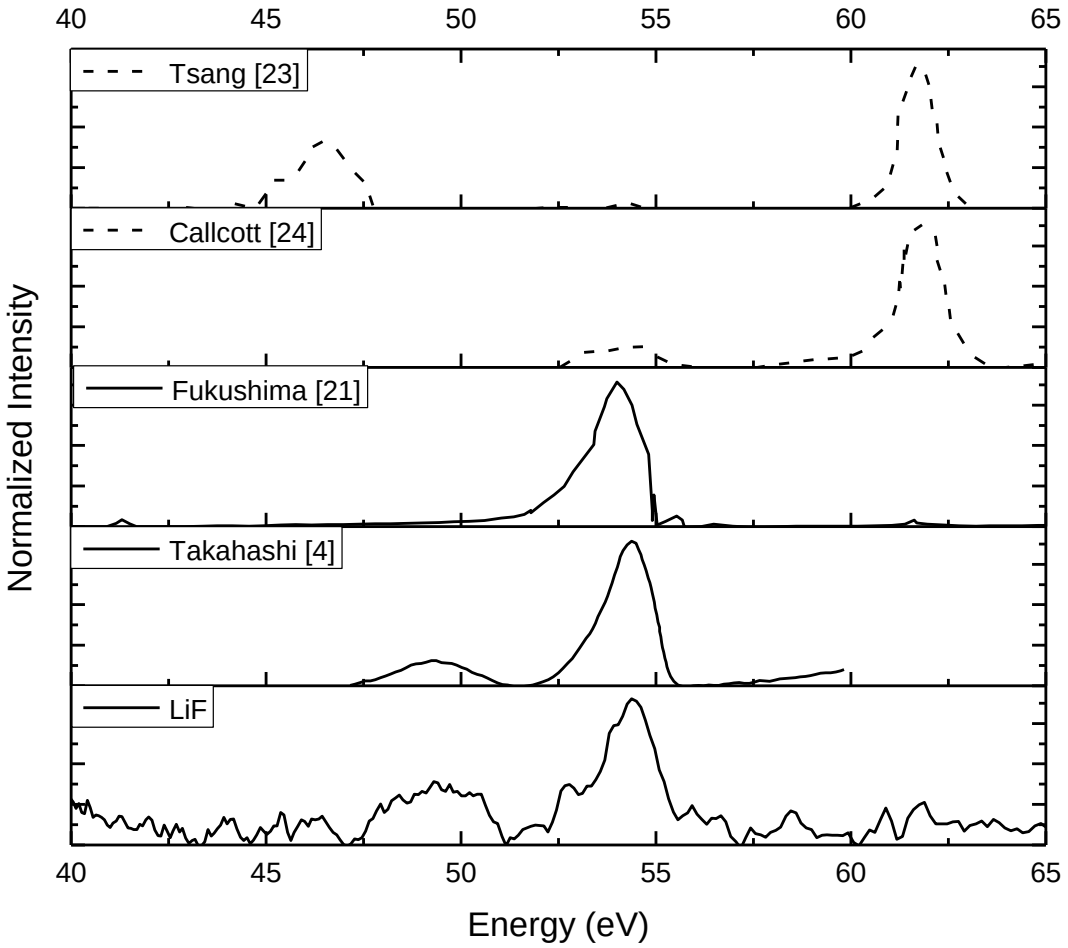

Figure 8: Comparison of the Li Kα emission in LiF, between our measurement "LiF" (2 kV, 50 nA and 300 s), spectra from Takahashi et al. [4], Fukushima et al. [25], Callcott [28], and Tsang [27]. The dashed curves represent the experiments with photon excitation, while the solid line curves represent electron excitation.

Figure 8 shows the spectra of LiF obtained with different instruments and under different excitation (electron, photon). Our spectrum shows two emission bands as observed by Takahashi *et al.* [4], one at a lower energy (from 47 eV to 51 eV) and the other at a higher energy (centered at 54.3 eV). The lower energy band is attributed to the emission of Li Kα from lithium oxide [2]. This is emphasized by the increasing intensity of this band with time, simultaneously to that of the O Kα emission, while the intensity of the F Kα emission is decreasing, as depicted in Fig. 9. The absence of the oxide emission in the work of Fukushima *et al.* [25] can be due to Ar^+ ion sputtering of the surface that prevents the oxidation of the lithium. The higher energy band, around 54 eV, is attributed to the emission from lithium metal that has accumulated at the surface of the sample after the removal of fluorine under the beam damage. On the other side, using photon excitation, Callcott *et al.* [28] observed in his work a similar emission band around 61 eV to the one reported by Tsang *et al.* [27]. In Tsang's work, the emission band centered at 46.5 eV, absent from the observations under electron excitation, was attributed to the valence band-core transition, while the one at 61 eV was ascribed to excitonic origin.

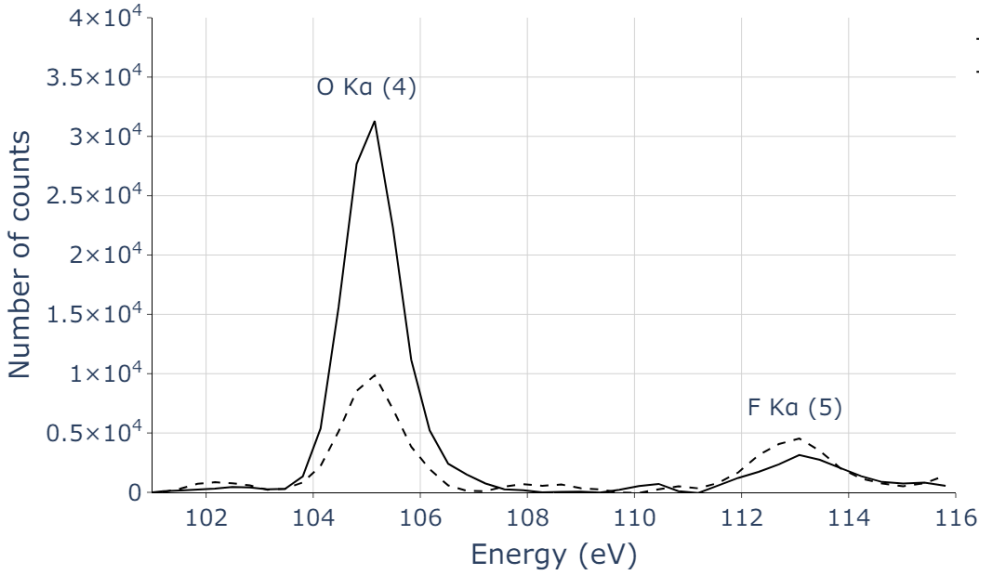

Figure 9: O Kα (m = 4) and F Kα (m = 5) emissions, observed on a LiF sample, as a function of the acquisition time (dashed line after 400 s, solid line after 1200 s). The numbers in parentheses are the diffraction orders.

- *$LiNbO_3$*

Figure 10 shows the spectrum of a $LiNbO_3$ crystal within the energy range from 40 eV to 110 eV. The spectrum reveals the presence of the 2nd, 3rd, and 4th diffraction orders of the Nb Mζ emission at approximately 85 eV, 56 eV and 42 eV, respectively, in addition to the high diffraction orders of the O K emission (5th to 12th order). It is important to mention that there was no observation of high orders of C Kα in the spectrum. A zoom on the range from 49 eV to 62 eV is presented in Fig. 11. The peak centered at around 54.7 eV could be attributed to Li Kα, similar to what was reported by Fukushima *et al.*[25]. While the other peaks are more intense and better resolved compared to Fukushima's work, the Li Kα peak is still low. This fact can be explained by the strong self-absorption of the Li Kα radiation, as detailed in Table 2, which decreases the available signal, limiting the sensitivity. To optimize the detection of the emission band within the Li K region for this sample, it was essential to extend the acquisition time to 600 s, in that way augmenting counting statistics and enhancing the signal-to-noise ratio. However, the extended exposure may lead to sample damage due to radiation effects.

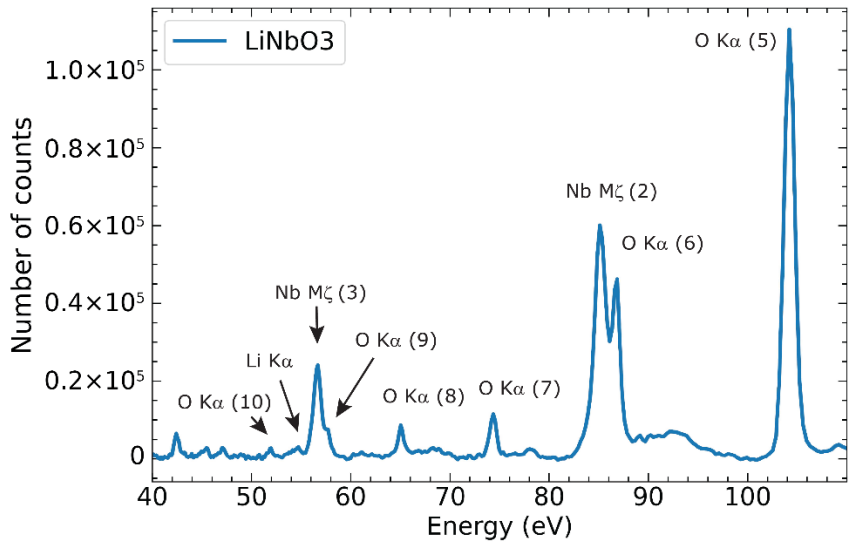

Figure 10: Spectrum of $LiNbO_3$, measured under conditions of 5 kV, 100 nA, 600 s.

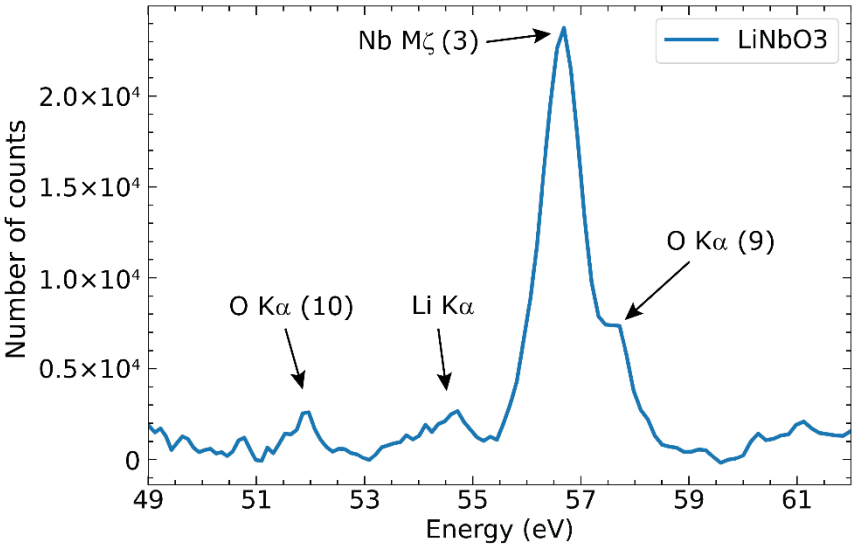

Figure 11: Zoom of the $LiNbO_3$ spectrum on the region from 49 eV to 62 eV.

- *Lithium-bearing minerals*

Table 2 shows that the attenuation lengths of a 50 eV radiation do not exceed 25 nm for silicates, meaning that the characteristic line of Li will be rapidly attenuated within the sample. Hence, the measurement of emission from Li atoms is difficult and only possible at a low sensitivity of detection (low intensity and poor peak-to-background ratio). Anyway, attempts to acquire the Li Kα emission in the lithium bearing minerals were made. The analyzed samples include lepidolite, amblygonite and bikitaïte. In the following, only amblygonite will be discussed exemplarily, since the difficulties in the other samples were the same. Figure 12 shows the measured spectrum of amblygonite in the full range of the spectrometer. The analysis was performed using a low accelerating voltage of 3 kV, a beam current of 200 nA and an acquisition time of 200 s. The spectrum presents the emission of O Kα, Al $L_{2,3}$, and P $L_{2,3}$ with no significant evidence of carbon contamination. A zoom on the range from 48 eV to 72 eV is plotted in Fig. 13.

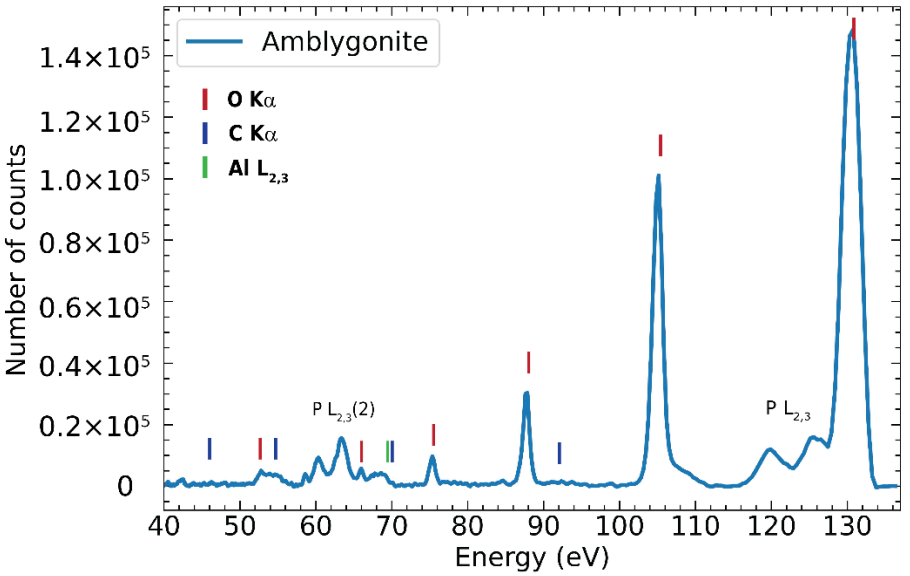

Figure 12: Full amblygonite spectrum; the vertical lines give the energies of the O Kα (red), C Kα (blue) and Al $L_{2,3}$ (green) emissions with their high diffraction orders.

Figure 13 illustrates the potential overlap between the second-order emission of P $L_{2,3}$ and Li Kα, as determined through density functional theory (DFT) calculations, in comparison to the experimental spectrum. The simulated spectrum, deduced from the valence density of states, is aligned on the experimental spectrum by choosing the energy of the main peak as 64.5 eV, The three curves are normalized to their maximum at (54 – 55) eV. The emission band centered at 54 eV, and extending from around 52 eV to 56 eV, presents possible overlaps of different emission: Li Kα, the lower energy secondary peak of P $L_{2,3}$ (m = 2) around 54.5 eV and O Kα (m = 10) around 53 eV.

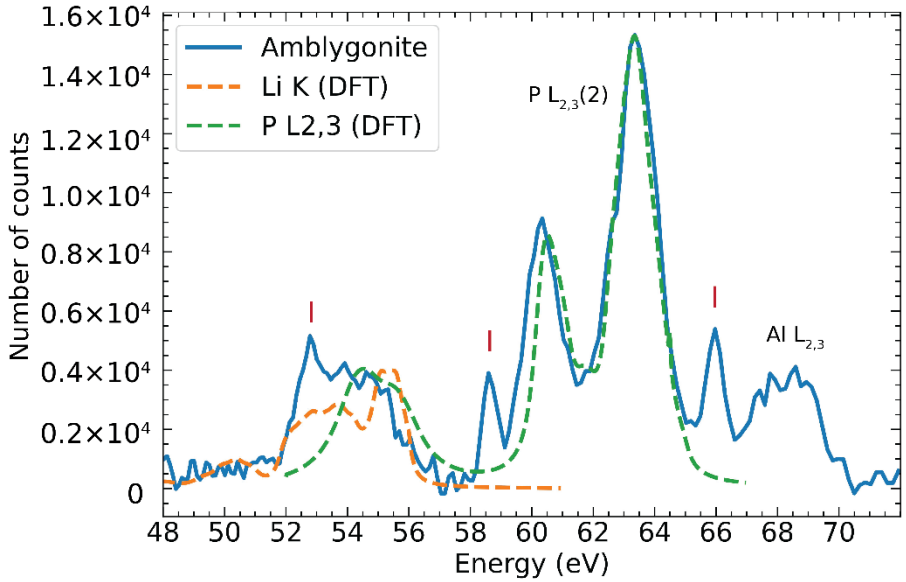

Figure 13: Experimental amblygonite spectrum (blue), compared with DFT calculations of P $L_{2,3}$ (green) and Li Kα (orange). The red vertical lines represent the positions of the high diffraction orders of O Kα emission.

Several peaks were easily resolved, such as Al $L_{2,3}$, P $L_{2,3}$, O Kα, etc. For lithium however, several difficulties were encountered, including the overlap of high diffraction order emission from elements present in the sample, such as Si $L_{2,3}$ (for lepidolite and bikitaïte), P $L_{2,3}$ (for

amblygonite) and O Kα. In addition, an overlap with high diffraction order emissions from the presence of external contaminations such as C Kα (for lepidolite and bikitaïte), coming from the decomposition of hydrocarbons under irradiation, is observed. Furthermore, a change of the spectrum with time under influence of the beam has been observed.

Conclusion

In this work, we have succeeded to setup the newly developed RZP spectrometer on an EPMA. The spectrometer covers the soft x-ray range of (35 – 130) eV, with a resolution reaching 0.3 eV measured at the Al $L_{2,3}$ edge. This high resolution allows the determination of the fine features of the emission bands in this range, accompanied by a high signal-to-noise ratio. We presented Li Kα emission acquired in different compounds including Li metal, LiF and $LiNbO_3$, providing valuable insights into the chemical behavior of lithium in different environment. We discussed the difficulties confronted when analyzing complex materials such as the lithium bearing minerals. The demonstrated capabilities of the RZP spectrometer open the gate for future research in the field of x-ray emission spectroscopy and for the quantification of lithium.

Acknowledgments

This research was funded by Agence Nationale de la Recherche in the framework of the SQLX Project (ANR-20-CE29-0022). This work would not have been possible without the pioneering work of the regretful Alexei Erko on the use of reflection zone plates. We also thank Dr. Jean-Louis Longuet from CEA, Dr. Colin MacRae and Dr. Nick Wilson from CSIRO Minerals, Pr. Raynald Gauvin from McGill University, Dr. Marie-Christine Lépy from CEA-LIST-LNE-LNHB and Mrs. Blandine Remy from Arcelor Mittal for their interesting discussions, the LCPMR intern, Wiam Aid for her participation in the experiments. Dr. Yuchun Tu from Shanghai Institute of Laser Plasma is thanked for providing us with the $LiNbO_3$ sample.

References

[1] K. Hassebi, K. Le Guen, N. Rividi, A. Verlaguet, and P. Jonnard, "Calculation of emission spectra of lithium compounds," *X-Ray Spectrometry*, vol. 52, no. 6, pp. 330–335, 2023, doi: 10.1002/xrs.3329.

[2] K. Mukai, R. Kasada, K. Sasaki, and S. Konishi, "Occupied Electronic States of Li in Li, Li2O2 , and Li2O Analyzed by Soft X-ray Emission Spectroscopy," *J. Phys. Chem. C*, vol. 124, no. 17, pp. 9256–9260, Apr. 2020, doi: 10.1021/acs.jpcc.0c02885.

[3] M. Terauchi *et al.*, "Ultrasoft-X-ray emission spectroscopy using a newly designed wavelength-dispersive spectrometer attached to a transmission electron microscope," *Journal of Electron Microscopy*, vol. 61, no. 1, pp. 1–8, Feb. 2012, doi: 10.1093/jmicro/dfr076.

[4] H. Takahashi *et al.*, "Development of soft X-ray emission spectrometer for EPMA/SEM and its application," *IOP Conf. Ser.: Mater. Sci. Eng.*, vol. 109, p. 012017, Feb. 2016, doi: 10.1088/1757-899X/109/1/012017.

[1] R. Castaing, A. Guinier, in Proceedings of the Conference on Electron Microscopy (Delft, Martinus Nijhoff, 1949), pp. 60–63.

[6] Y. Kubo, K. Hamada, and A. Urano, "Minimum detection limit and spatial resolution of thin-sample field-emission electron probe microanalysis," *Ultramicroscopy*, vol. 135, pp. 64–70, Dec. 2013, doi: 10.1016/j.ultramic.2013.05.011.

[7] M. Terauchi and M. Kawana, “Soft-X-ray emission spectroscopy based on TEM—Toward a total electronic structure analysis,” *Ultramicroscopy*, vol. 106, no. 11–12, pp. 1069–1075, Oct. 2006, doi: 10.1016/j.ultramic.2006.04.021.
[8] C. Bonnelle, “Chapter 7. X-Ray spectroscopy,” *Annu. Rep. Prog. Chem., Sect. C*, vol. 84, p. 201, 1987, doi: 10.1039/pc9878400201.
[9] S. Burgess, X. Li, and J. Holland, “High spatial resolution energy dispersive X-ray spectrometry in the SEM and the detection of light elements including lithium,” p. 5, 2013.
[10] P. Hovington *et al.*, “Can we detect Li K X-ray in lithium compounds using energy dispersive spectroscopy?,” *Scanning*, vol. 38, no. 6, pp. 571–578, Nov. 2016, doi: 10.1002/sca.21302.
[11] O. Aita and T. Sagawa, “Soft X-Ray Emission Spectra of Light Elements. I. Li, Be, B, Al and Si,” *J. Phys. Soc. Jpn.*, vol. 27, no. 1, pp. 164–175, Jul. 1969, doi: 10.1143/JPSJ.27.164.
[12] A. Erko, A. Firsov, and F. Senf, “Novel parallel vacuum ultra-violet/X-ray fluorescence spectrometer,” *Spectrochimica Acta Part B: Atomic Spectroscopy*, vol. 67, pp. 57–63, Jan. 2012, doi: 10.1016/j.sab.2012.01.001.
[13] A. Erko *et al.*, “New parallel wavelength-dispersive spectrometer based on scanning electron microscope,” *Opt. Express*, vol. 22, no. 14, p. 16897, Jul. 2014, doi: 10.1364/OE.22.016897.
[14] A. Hafner *et al.*, “Reflection zone plate wavelength-dispersive spectrometer for ultra-light elements measurements,” *Opt. Express*, vol. 23, no. 23, p. 29476, Nov. 2015, doi: 10.1364/OE.23.029476.
[15] Z. Yin *et al.*, “Highly efficient soft X-ray spectrometer based on a reflection zone plate for resonant inelastic X-ray scattering measurements,” *Opt. Express*, vol. 25, no. 10, p. 10984, May 2017, doi: 10.1364/OE.25.010984.
[16] J. Probst, C. Braig, and A. Erko, “Flat Field Soft X-ray Spectrometry with Reflection Zone Plates on a Curved Substrate,” *Applied Sciences*, vol. 10, no. 20, p. 7210, Oct. 2020, doi: 10.3390/app10207210.
[17] C. Braig *et al.*, “Design and optimization of a parallel spectrometer for ultra-fast X-ray science,” *Opt. Express*, vol. 22, no. 10, p. 12583, May 2014, doi: 10.1364/OE.22.012583.
[18] S.-J. Baek, A. Park, Y.-J. Ahn, and J. Choo, “Baseline correction using asymmetrically reweighted penalized least squares smoothing,” *Analyst*, vol. 140, no. 1, pp. 250–257, 2015, doi: 10.1039/C4AN01061B.
[19] P. Jonnard and C. Bonnelle, “Cauchois and Sénémaud Tables of wavelengths of X-ray emission lines and absorption edges,” *X-Ray Spectrometry*, vol. 40, no. 1, pp. 12–16, 2011, doi: 10.1002/xrs.1293.
[20] B. L. Henke, E. M. Gullikson, and J. C. Davis, “X-Ray Interactions: Photoabsorption, Scattering, Transmission, and Reflection at E = 50-30,000 eV, Z = 1-92,” *Atomic Data and Nuclear Data Tables*, vol. 54, no. 2, pp. 181–342, Jul. 1993, doi: 10.1006/adnd.1993.1013.
[21] P. Blaha, K. Schwarz, F. Tran, R. Laskowski, G. K. H. Madsen, and L. D. Marks, “WIEN2k: An APW+lo program for calculating the properties of solids,” *J. Chem. Phys.*, vol. 152, no. 7, p. 074101, Feb. 2020, doi: 10.1063/1.5143061.
[22] S. Cottenier, “Density Functional Theory and the Family of (L)APW-methods: a step-by-step introduction”.
[23] J. P. Perdew, K. Burke, and M. Ernzerhof, “Generalized Gradient Approximation Made Simple,” *Phys. Rev. Lett.*, vol. 77, no. 18, pp. 3865–3868, Oct. 1996, doi: 10.1103/PhysRevLett.77.3865.
[24] J. R. Hoenigman and R. G. Keil, “An XPS study of the adsorption of oxygen and water vapor on clean lithium films,” *Applications of Surface Science*, vol. 18, no. 1, pp. 207–222, May 1984, doi: 10.1016/0378-5963(84)90045-X.
[25] S. Fukushima, T. Ogiwara, T. Kimura, K. Tsukamoto, T. Tazawa, and S. Tanuma, “The intensity changes of ultra-soft X-ray spectra of several light element oxides,” *Microsc Microanal*, vol. 14, no. S2, pp. 1286–1287, Aug. 2008, doi: 10.1017/S1431927608084390.

[26] E. T. Arakawa and M. W. Williams, “Radiative Decay of Core Excitons in Alkali Halides,” *Phys. Rev. Lett.*, vol. 36, no. 6, pp. 333–336, Feb. 1976, doi: 10.1103/PhysRevLett.36.333.

[27] K. L. Tsang, C. H. Zhang, T. A. Callcott, E. T. Arakawa, and D. L. Ederer, “Fluorescent emission spectra of lithium fluoride with use of synchrotron radiation,” *Phys. Rev. B*, vol. 35, no. 16, pp. 8374–8377, Jun. 1987, doi: 10.1103/PhysRevB.35.8374.

[28] T. A. Callcott, K. L. Tsang, C. H. Zhang, D. L. Ederer, and E. T. Arakawa, “High-efficiency soft x-ray emission spectrometer for use with synchrotron radiation excitation,” *Review of Scientific Instruments*, vol. 57, no. 11, pp. 2680–2690, Nov. 1986, doi: 10.1063/1.1139078.